

## Model-based development of a compliant locomotion system for a small scout rover

Leon Stubbig<sup>1,2</sup>, Roy Lichtenheldt<sup>1</sup>, Felix Becker<sup>2</sup>, Klaus Zimmermann<sup>2</sup>

<sup>1</sup> German Aerospace Center (DLR), Institute of System Dynamics and Control

<sup>2</sup> Technische Universität Ilmenau, Technical Mechanics Group

### ABSTRACT

All currently active planetary exploration robots employ wheels for locomotion. In this work an alternative robotic locomotion concept is examined: the rimless wheel, also known as whegs. It has been proven to be successful in traversing rough terrain on earth and inhibits an appealing simplicity in its mechanics and controls. These aspects along with its inherent redundancy make the rimless wheel particularly suited for planetary exploration. The rimless wheel's kinematics and compliant spokes are analytically examined using mechanical models. The dynamics of these models are explored in a computational multi-body simulation which confirms the conclusions drawn from the analytical models about running, climbing and movement on rough terrain. A parameter variation then yields a set of suitable parameters for a future scout rover. The application in sand is considered separately both analytically and computationally. Based on these results a single wheel is build and tested on the conclusions drawn from modelling and simulation. These experiments provide strong support that the two-sided goal of efficient movement on hard and flat surfaces as well as reliable negotiation of rough terrain can be achieved with the developed locomotion system.

**Index Terms** - Robotic locomotion, planetary exploration, small rovers, rimless wheels, whegs, compliant mechanisms, multi-body simulations

### 1. INTRODUCTION

Since the first successful landing of a rover on the moon in 1971 (Lunokhod 1), remote controlled robots are a key part of planetary exploration. In contrast to telescopes and space probes rovers are able to examine planetary bodies at close range. The capability to take images and investigate samples from different locations make rovers an invaluable tool for planetary scientists. So far planetary exploration robots have mainly relied on mobility systems based on wheels [2]. Due to the danger of getting stuck between rocks or in soft soil they have to be operated slowly and carefully which means that many scientifically interesting areas remain unexplored. For example, water ice is known to exist in craters in the moon's polar regions [3] and if life has ever



Figure 1: Three areas that cannot be explored by current rovers: The Cisternazza crater on Mt. Etna (left), the rocky martian surface as seen by the Mars Pathfinder Lander (1997) [1] (center), a rough passage in a lava tube too narrow for humans (right)

existed on Mars it might have endured in caves [4]. Furthermore, there are a number of mission concepts that require robust locomotion for smaller exploration robots [5]. They can assist a main rover in assessing terrain traversability [6], fetch samples [7] [8] or form logistic chains [9]. Other concepts promote swarm exploration strategies that consist of cooperating small robots only [10]. An often discussed approach to improve rough terrain capabilities is legged locomotion [11] [12] [13]. These concepts are often biologically inspired and aim to replicate the impressive motion capabilities of different animals. The number of degrees of freedom in a robotic legs are not only an advantage though. They also greatly complicate the mechanism's control, reduce energy density and efficiency, and increase the number of single points of failure. In this work an alternative concept to robot mobility is examined: the rimless wheel, see Fig. 2. The robots Whegs [14] and RHex [15] were the first to employ rimless wheels and it has since been successfully applied in a number of research robots [7] [8] [9] [16]. Conceptually a rimless wheel is created by removing the mantle of a spoked wheel. The resulting mechanism is a cross between wheels and legs in that it moves in discrete steps but still performs full wheel revolutions, where the former eliminates the need for a continuous track and the latter greatly simplifies the mechanism and its control.

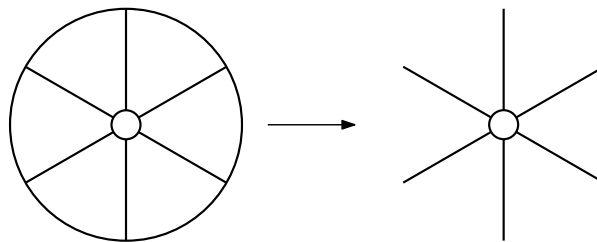


Figure 2: The rimless wheel is created by removing the mantle of a spoked wheel

The objective is therefore to design a locomotion system based on the rimless wheel concept that can negotiate sandy and rough terrain in planetary exploration scenarios as exemplified in Fig.1. It has to be reliable, robust and efficient. This goal is approached in a number of steps: First, the rimless wheel's kinematics and compliant spokes are examined using mechanical models. Second, the dynamics of these models are explored in a computational multi-body simulation and a parameter variation yields a set of suitable parameters for a future scout rover. Then the application in sand is considered separately both analytically and computationally. Based on these results a single wheel is built and tested on the conclusions drawn from modelling and simulation.

## 2. RIMLESS WHEEL KINEMATICS

The following section highlights the most important characteristics of rimless wheel locomotion and compares them to those of a “conventional wheel”. The models are all based on quasi-static relations and lead to a favourable wheel configuration.

Assuming no slip and rigid spokes, the forward velocity of a moving rimless wheel can be derived by examining a rolling polygon as shown in Fig. 3a. Every wheel revolution causes a forward movement of the length of the polygon's circumference  $U$ :

$$v = \frac{\omega U}{2\pi} = \frac{1}{\pi} \omega n l \sin\left(\frac{\pi}{n}\right), \quad (1)$$

where  $n$  is the number of spokes,  $l$  is spoke length,  $v$  is the robot's forward speed and  $\omega$  is the angular wheel velocity.

In contrast to a conventional wheel the rimless wheel can climb obstacles higher than its hub. During every wheel revolution the spokes reach high above the wheel hub and can gain traction

on top of obstacles, as sketched in Figs 3b and 3c. Assuming rigid spokes and a vertical orientation of the spoke in contact the maximum height that one wheel can reach is [14]:

$$h = l + l \sin \left( \alpha - \frac{\pi}{2} \right), \quad (2)$$

where  $h$  is obstacle height,  $l$  is spoke length and  $\alpha$  is the angle between spokes ( $\alpha = \frac{2\pi}{n}$ ), assuming an even distribution around the wheel hub. A wheel position slightly tilted backwards reaches marginally higher but is unlikely to be attained during operation. Fig. 5 shows climbable obstacle height relative to spoke length for a range of spokes per wheel.

The walking-like locomotion of rimless wheels is advantageous for obstacle climbing and movement on rough terrain. This benefit comes with trade-offs though. One of these drawbacks are the vertical movements the wheel's hub experiences at every step, see Fig. 4.

For a rigid wheel this movement can be described as an inverted pendulum with the hub moving on a circular arc around the foothold. The height of the arc's sagitta depends on spoke length  $l$  and the angle between adjacent spokes  $\alpha$ :

$$\Delta h = l \left[ 1 - \cos \left( \frac{\alpha}{2} \right) \right]. \quad (3)$$

The first robot based on rimless wheels, Whegs I [14], relied on this consideration. The two-dimensional path of the wheel's hub can also be calculated directly using

$$y = \sqrt{l^2 - (x - kw)^2}; k = \left\lfloor \frac{x}{w} \right\rfloor, \quad (4)$$

where  $l$  spoke length,  $w$  is step length ( $w = \frac{U}{n}$ ), and  $k$  is an integer factor that is incremented when a new spokes comes in contact ( $k = 0, 1, 2, \dots$ ).

The magnitude of hub movements is reduced for radially compliant spokes. This is a result of the radial spring relaxing when being tilted. The hub reaches its highest point when the spoke in contact is oriented vertically and its lowest point when two spokes are symmetrically in contact. The difference can be calculated as

$$\Delta h = l_0 \left[ 1 - \cos \left( \frac{\alpha}{2} \right) \right] - \frac{mg}{2c_r}, \quad (5)$$

where  $l_0$  is the compliant spoke's uncompressed length,  $m$  is the mass supported by the spoke,  $g$  is acceleration of gravity and  $c_r$  is spring stiffness.

The effect can be seen in Fig. 6 which plots the relative vertical hub movement of a rigid and two compliant wheels. Relative vertical hub movement is defined as the magnitude of hub movement relative to hub height when the spoke in contact is oriented vertically. As the hub movement

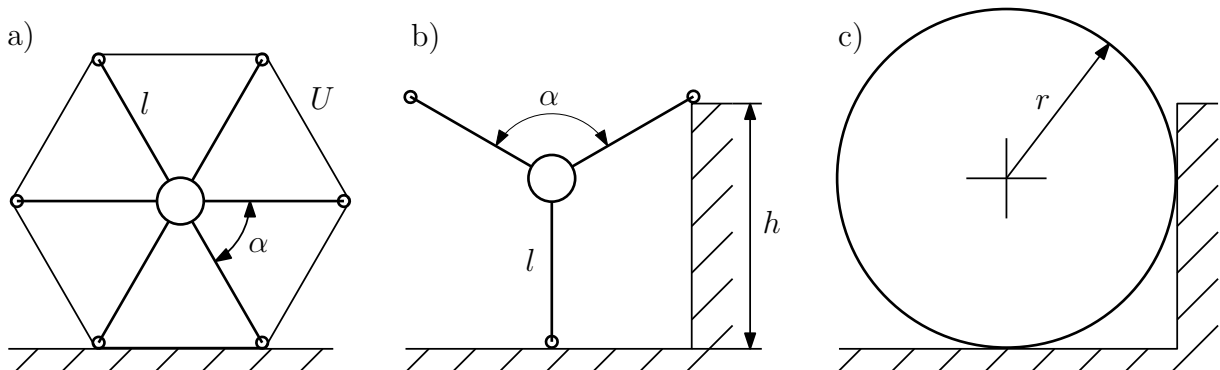


Figure 3: Rimless wheel kinematics and a conventional wheel of comparable size ( $l = r$ )

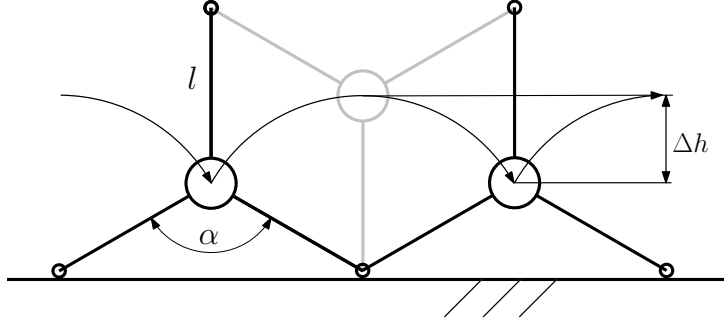


Figure 4: Vertical hub movement of a rimless wheel ( $n = 3$ )

of a wheel with two spokes is always 100 % the plots start with  $n = 3$ , where the relative hub movement is 50 % for all cases. Here the wheel is rotated to exactly half of its initial height ( $\cos(\pi/3) = 0.5$ ). Therefore the lowered maximum hub height and the spring relaxation cancel out. Thus, a compliant spoke is beneficial in reducing hub movements for wheels with four or more spokes. A lower stiffness increases the effect.

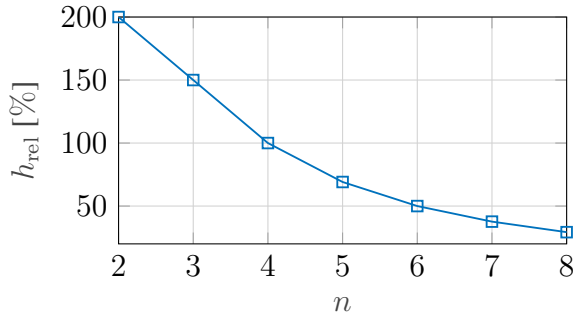


Figure 5: Maximum climbable step obstacle height relative to spoke length for a different number of spokes

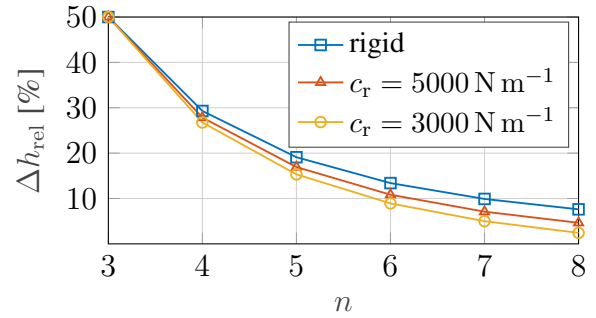


Figure 6: Comparison of relative hub movement for rigid and compliant spokes ( $m = 5 \text{ kg}$ ,  $g = 9.81 \text{ N kg}^{-1}$ )

The examination of rimless wheel kinematics allows the selection of a preferred wheel configuration. It is shown in Fig. 7 and consists of two wheels à three spokes that are operated with a  $60^\circ$  phase offset. Together with inertial effects this allows the axis to be treated like a six spoke wheel when calculating hub movements (13.4 %  $l$  for rigid spokes). For the negotiation of rough terrain and step obstacles the two wheels can be brought into phase by either passive mechanics or a suitable controller. The envisioned scout rover can consist of two, three or more of these axis.

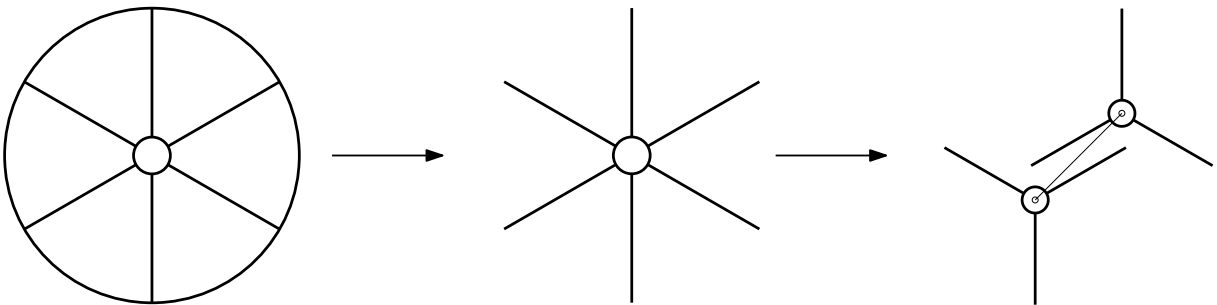


Figure 7: One rimless wheel with six spokes is split into two wheels with three spokes

### 3. COMPLIANT SPOKE MODELLING

Rimless wheels are well suited for the application at hand. The envisioned scout rover has to cope with rough terrain where good obstacle climbing is crucial. The concept is improved by the introduction of compliant spokes. The whole mobility system gains robustness as shock loads

are absorbed and, as shown before, hub movements are reduced. Additionally the efficiency of locomotion can potentially be improved by the properly timed periodic storage and release of mechanical energy in the deformation of elastic spokes. Table 1 lists the advantages and disadvantages of compliant wheels more comprisingly.

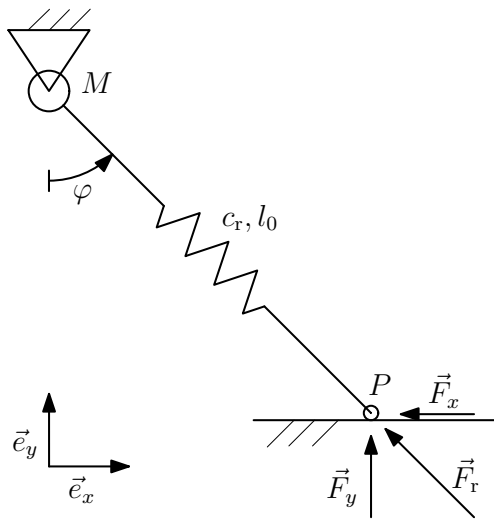
Table 1: Characteristics of compliant spokes

Advantages	Disadvantages
+ robust against shock loads and falls	– possibly detrimental resonance effects
+ dynamic energy storage	– more intricate design than rigid spokes
+ lighter design through function integration	– directional properties possible
+ reduced hub movements	
+ adaptation to uneven terrain	
+ controllable movement at high speeds	
due to lower hub movements and shock loads	
+ reduced storage space (foldable)	

Different ways of implementing compliance into a spoke are examined in terms of their reaction forces and behaviour under load. This is done using three spoke models, termed Radial Spring Model, Torsion Spring Model and Continuous Beam Model, which were chosen to represent different mechanical options available to achieve compliance in a radial direction.

The Radial Spring Model is the simplest, most reduced model that incorporates radial compliance. It consists of a linear spring located between hub and foot and is ideally stiff in the tangential direction. When the spoke is deformed the spring causes a radial reaction force that points towards the hub, as shown in Fig. 8.

The radial ground reaction force  $F_r$  can be calculated by Equation 6, where  $M$  and  $P$  are the position of hinge and foot, respectively,  $c_r$  is radial stiffness and  $l_0$  is uncompressed spoke length. The radial force  $F_r$  can then be split into its horizontal and vertical components  $F_x$  and  $F_y$  using the spoke angle  $\varphi$ , see Equations 7 to 9.



$$F_r = c_r \left( l_0 - \sqrt{(x_P - x_M)^2 + (y_P - y_M)^2} \right) \quad (6)$$

$$\varphi = \tan^{-1} \left( \frac{x_P - x_M}{y_P - y_M} \right) \quad (7)$$

$$F_x = F_r \sin \varphi \quad (8)$$

$$F_y = F_r \cos \varphi \quad (9)$$

Figure 8: Radial Spring Model

The second considered way of giving the spoke compliance is the introduction of a joint and torsion spring in the spoke's middle. Segmented legs are considered quite frequently in robotics research because they are similar to the legs of walking animals (e.g. [17] [18]) and recently the passively compliant version has been subject to research as well [19].

Fig. 9 shows sketches of the model and the respective free body diagrams. The spoke consists

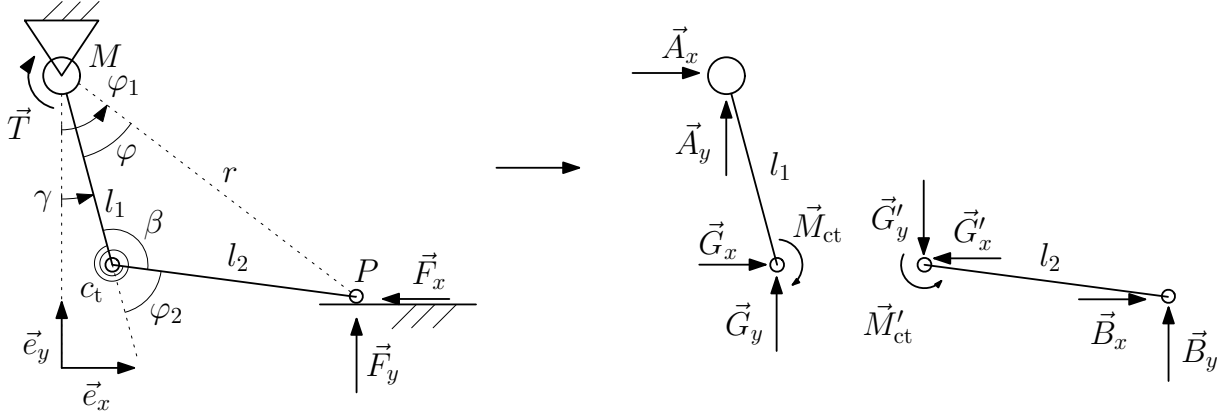


Figure 9: Torsion spring model and free body diagrams

of two segments of lengths  $l_1$  and  $l_2$  that are connected by a torsion spring of stiffness  $c_t$ . The equilibrium conditions reduce to

$$A_x + B_x = A_y + B_y = 0 \quad (10)$$

$$-T - M_{ct} - A_x l_1 \cos \varphi_1 - A_y l_1 \sin \varphi_1 = 0 \quad (11)$$

$$M'_{ct} + B_x l_2 \cos(\varphi_1 + \varphi_2) + B_y l_2 \sin(\varphi_1 + \varphi_2) = 0. \quad (12)$$

This linear system of four equations has four unknowns (the joint forces  $A_x, A_y, B_x$  and  $B_y$ ) and has a unique analytical solution. The spring torque  $M_{ct}$  can be calculated ahead as it is only depending on the model's position:

$$M_{ct} = -c_t(\varphi_2 - \varphi_{20}), \quad (13)$$

where  $c_t$  is spring constant,  $\varphi_2$  is spring deflection and  $\varphi_{20}$  is the spring's rest angle.

Assuming a clockwise turning of the spoke the marked angles can be uniquely calculated using the laws of sines and cosines and the PYTHAGOREAN theorem, see Equations 14. Without this constraint there would be two spoke configurations for every foot position ( $\varphi_2$  and  $-\varphi_2$ ).

$$\begin{aligned} r &= \sqrt{(x_P - x_M)^2 + (y_P - y_M)^2} & \gamma &= -\arctan\left(\frac{x_P - x_M}{y_P - y_M}\right) \\ \beta &= \arccos\left(\frac{-r^2 + l_1^2 + l_2^2}{2l_1 l_2}\right) & \varphi &= \arcsin\left(\frac{l_2 \sin \beta}{r}\right) \\ \varphi_2 &= \pi - \beta & \varphi_1 &= \gamma - \varphi \end{aligned} \quad (14)$$

Several differences to the Radial Spring Model can be identified. First, the model's non-linear geometry causes a degressive radial spring characteristic. The stiffness therefore decreases when the spoke is deflected. Second, the spoke loses the ability to increase its length beyond a certain point. When the two segments are fully aligned all forces applied by a tensional load will be absorbed in the joints. When the robot pulls itself up during obstacle climbing this behaviour has advantages.

Plotting the ground reaction forces spatially over a range of typical deformations, as shown in Fig. 10, provides an overview of the spoke's behaviour under load. Both horizontal and vertical force are zero on a circle of radius  $l_0$  around the hinge, i.e. when the spoke has its nominal length. Compressing the spoke leads to an increase in radial force that is split into its horizontal and vertical components depending on the spoke's angle.

Comparing the ground reaction forces for every point of the plotted area yields another insight. The foothold is lost when the horizontal component  $F_x$  is greater than vertical component  $F_y$

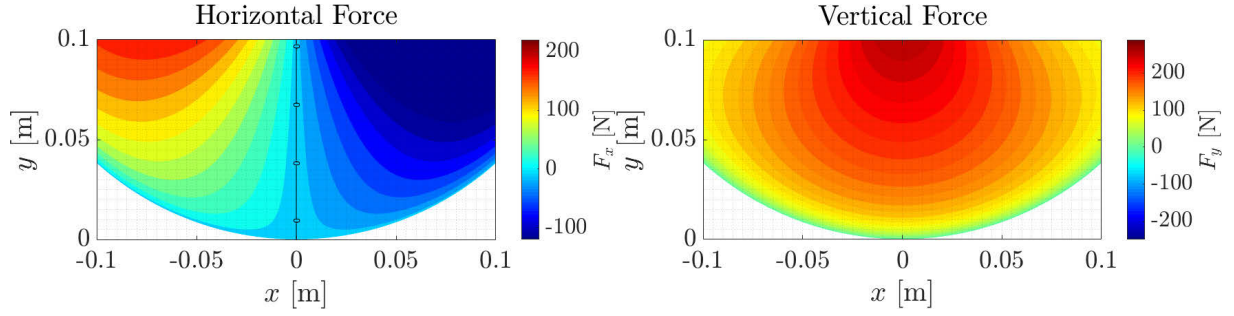


Figure 10: Exemplary ground reaction forces of the “Tosrion Spring Model”,  $(x_M, y_M) = (0, 0.15)$ ,  $T = 0 \text{ N m}$

times friction coefficient  $\mu$ :

$$F_x < \mu F_y. \quad (15)$$

This consideration based on COULOMB friction yields an operational range where the spoke can gain traction. Fig. 11 covers the same area as the preceding plot but all points where Equation 15 is not satisfied have been deleted. In the case of an unpowered spoke ( $T = 0 \text{ N m}$ ) the friction angle ( $\rho = \arctan \mu$ ) is a measure for this operational range which should be bigger than half the the angle between spokes ( $2\rho > \alpha$ ) to avoid recurring slipping and provide stable locomotion.

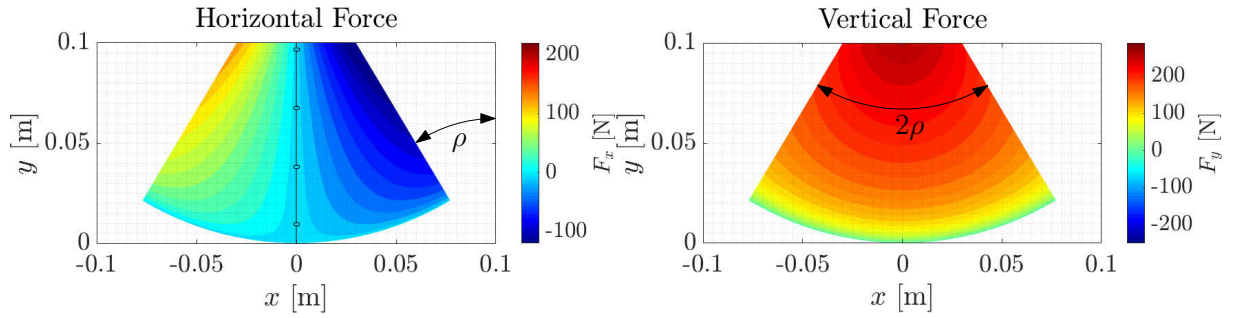


Figure 11: Range of stable footholds for  $\mu = 0.6$

The model’s radial stiffness characteristic can be tuned by changing the spring resting position  $\varphi_{20}$ , see Fig. 12. Here the radial reaction force ( $F_r = \sqrt{F_x^2 + F_y^2}$ ) is normalised with respect to a reference force at 10 % deformation.

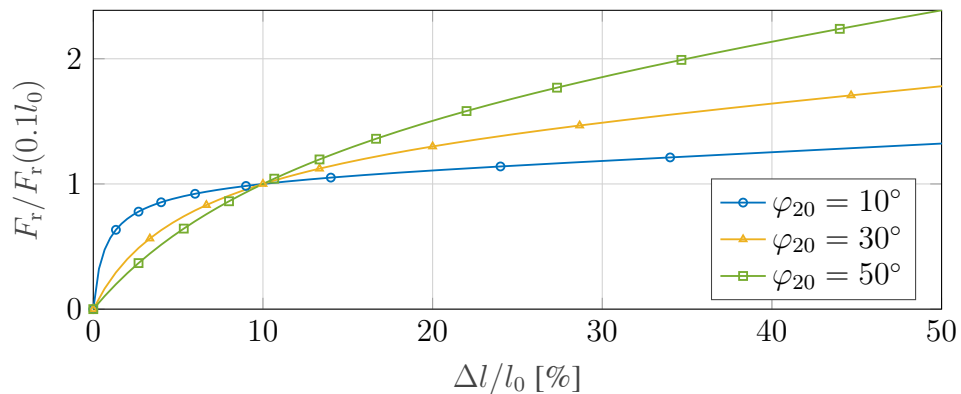


Figure 12: Radial reaction force for different spring rest angles  $\varphi_{20}$  and no torque

The third model consists of a curved, continuous beam that is deflected under a constant, vertical load, as shown in Fig. 13. The half-circle shape was first used in robotics as legs for RHex and has prevailed against a number of other leg designs [20]. In the presented model curvature is parametrised as it affects the non-linearity of the force-deflection curve in a fashion similar to the

segment angle in the Torsion Spring Model. The main idea is to develop two equivalent models for simulation and the prototype respectively.

The model shown in Fig. 13 is analysed using non-linear beam theory [21] to account for the expected large deformations. A number of assumptions have to be made for the calculation to be valid. These are in particular that the system is static, the beam's cross section is small in comparison to the other model dimensions, and the principle of SAINT-VENANT<sup>1</sup> as well as the hypothesis of BERNOULLI<sup>2</sup> are valid. HOOKE's law is assumed to apply to the material's elasticity.

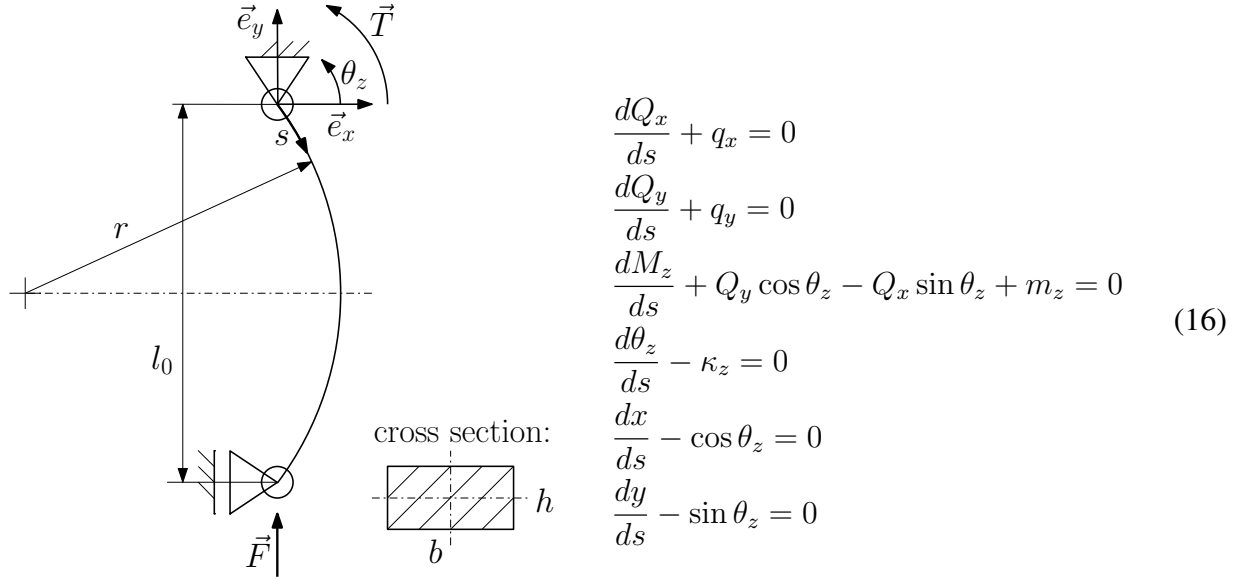


Figure 13: Continuous Spoke Model

The Continuous Beam Model is shown in Fig. 13. The model is two-dimensional and can be described in Cartesian coordinates by the set of differential equations listed next to it. Here  $Q_x$  and  $Q_y$  are lateral forces,  $s$  is the coordinate along the beam,  $q_x$ ,  $q_y$  and  $m_z$  are external loads,  $M_z$  is the bending moment along the beam and  $\theta_z$  is the angle of the beam's tangent at a point  $s$  measured relative to the  $x$ -axis. Furthermore, material laws provide the relation between curvature and bending torque  $M_z$ :

$$M_z = EI_z(\kappa_z - \kappa_{z0}). \tag{17}$$

where,  $E$  is YOUNG's modulus,  $I_z$  is the second moment of area, and  $\kappa_z$  and  $\kappa_{z0}$  are the beam's deformed and initial curvature, respectively.

Resulting from the modelled external loads the boundary conditions can be formulated as:

$$\begin{aligned}
 x(0) &= 0 & \frac{d\theta_z(0)}{ds} &= \frac{T}{EI_z} + \frac{1}{r} \\
 x(l) &= 0 & \frac{d\theta_z(l)}{ds} &= \frac{1}{r} \\
 y(0) &= 0 & & \\
 Q_y(l) &= F & &
 \end{aligned} \tag{18}$$

The resulting boundary value problem has no closed analytical solution and has to be solved numerically. Here the commercial computing environment Matlab (R2015b) was used. The deformation behaviour of an exemplary beam ( $l_0 = 0.15$  m,  $b = 8$  mm,  $h = 2.5$  mm,  $r = 0.1$  m,  $E = 210$  GPa,  $T = 0$  N m) is shown in Fig. 14 for increasing loads  $F$ . Varying the same beam's initial curvature changes the stiffness characteristic, as shown in Fig. 15. For increasing

<sup>1</sup>Stresses are distributed around the loading point as if the load would act on the full area.

<sup>2</sup>The beam's cross sections remain flat under load.



radii, the characteristic becomes more and more degressive.

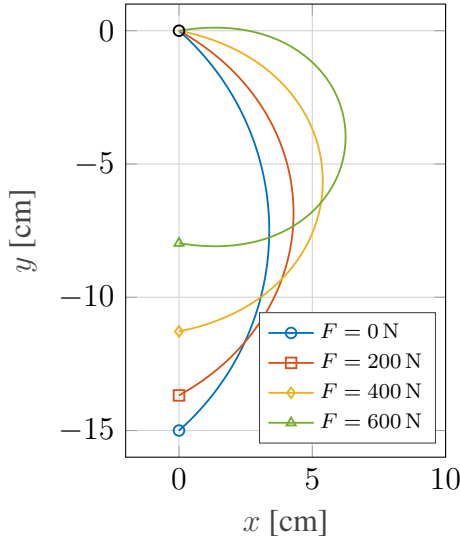


Figure 14: Deflection of the Continuous Beam Model

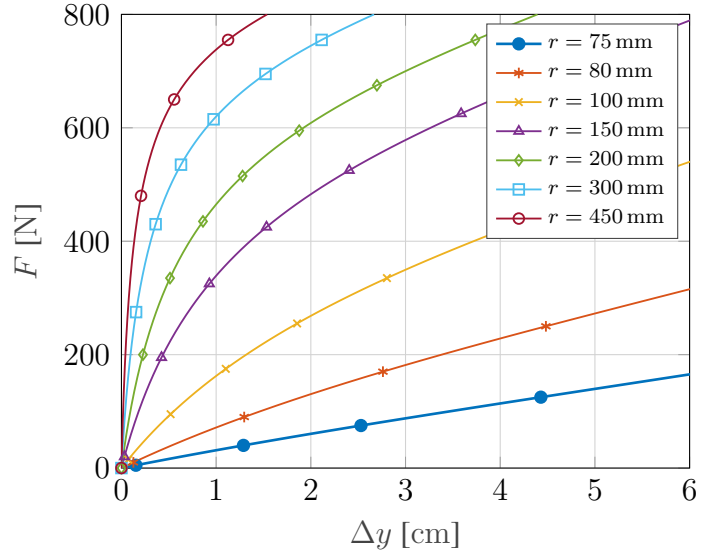


Figure 15: Radial force of a continuous spoke for different initial curvatures

Based on the revealed properties, the three analysed models have differing use in the following parts.

Starting the analysis of compliant spokes with the Radial Spring Model makes sense as it is the most reduced spoke model that incorporates compliance. It is also the only model suitable for analytical estimations of the dynamic properties of rimless wheel locomotion because of its constant stiffness [22] [23]. This is used in the following to estimate the system's resonant frequency.

The Torsion Spring Model and the Continuous Beam Model both inhibit degressive stiffness characteristics that are depending on the models' geometry. This equivalence is used in the following to set-up the simulation based on rigid-body mechanics, i.e. the Torsion Spring Model, and transfer the resulting spring characteristic into the Continuous Beam Model to design the prototype via fitting. This way the final spoke design can be monolithic and lightweight while the simulation can be efficiently performed using multi-body tools. The fitting process to achieve equal stiffness curves between the two models is briefly described in the following paragraph.

The Torsion Spring Model's stiffness is determined by two parameters: spring rest angle  $\varphi_{20}$  and torsion spring stiffness  $c_t$ . The Continuous Beam Model's stiffness on the other hand is defined by three parameters: thickness  $b$  and height  $h$  of the beam's cross section, and initial radius of curvature  $r$ . Therefore another condition is needed to distinctly transfer between the two. Here, this condition is derived from terramechanics: A spoke immersed in sand has to provide enough traction to move the robot, see Section 7. This consideration yields a minimum beam width and leaves two free parameters in each model for the fitting process. The shape of the stiffness curve is thereby determined by the models geometry,  $\varphi_{20}$  and  $r$  respectively. The absolute amount of force at a certain deformation is set by spring stiffness  $c_t$  and beam height  $h$ .

#### 4. MULTI-BODY SIMULATIONS

The dynamic behaviour of wheels equipped with compliant spokes is difficult to examine analytically. Applying for example the NEWTON-EULER equations to a rolling rimless wheel results in systems of discontinuous differential equations, which are only numerically solvable [24]. Thus, in this section the step is made away from analytical calculations to multi-body

simulations. This type of computational simulation models mechanical systems as rigid bodies that are connected by ideal joints, force relations and contact laws. The software is then able to derive the governing equations and solve them using a numerical integrator. Here the software tool Simpack (Release 9.9) is used.

The first simulation is dealing with step climbing. A single rimless wheel is free to move in a plane and is driven by a rheonomic joint of constant angular velocity. Maximum torque is limited by a custom, non-linear damper element. The step obstacle is the height of 1.5 times the spoke length, which is the expected maximum for climbable step height based on the analytical consideration for three spoked wheels, see Fig. 5. Frames from the simulations with rigid and compliant spokes are shown in Fig. 16. The angular wheel velocity is set to  $\omega = 1 \text{ rad s}^{-1}$  for all simulations and contacts are activated for the feet as well as the spokes (Elastic Layer Contact [25]).

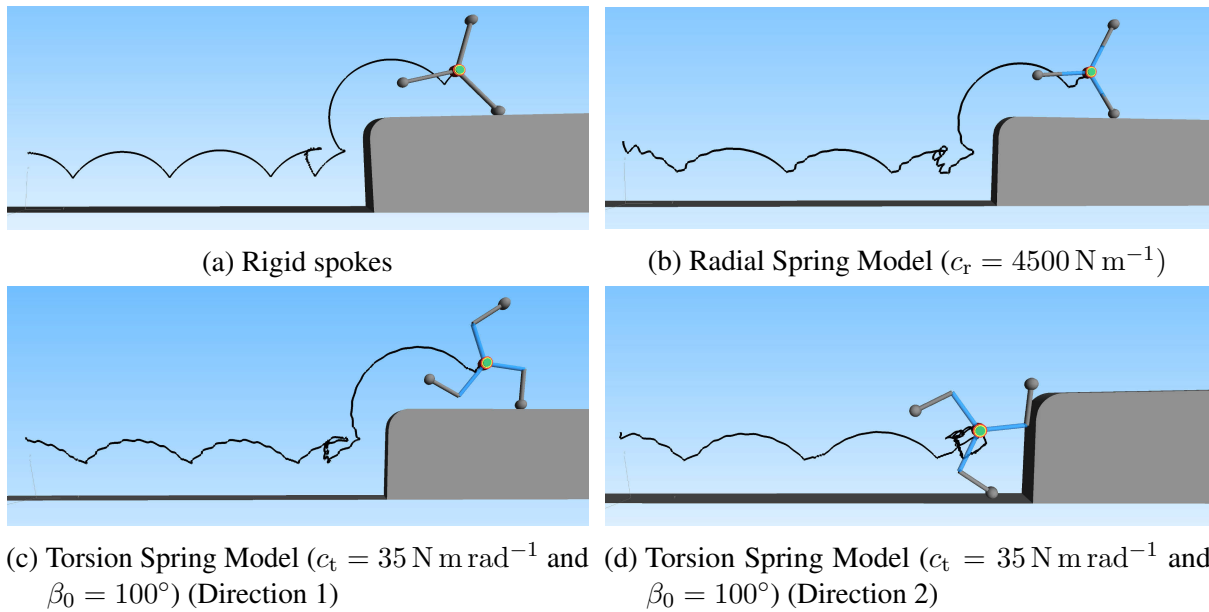


Figure 16: Rigid and compliant rimless wheels climb a step obstacle

All three wheels are able to surmount the step although the segmented spoke is only able to do so in Direction 1. After being turned the protruding knee pushes the wheel too far away from the obstacle for the foot to establish a foothold on top of the step.

The second computational experiment concerns hub movements. A rigid and a compliant wheel are simulated at a slow speed ( $\omega = 0.1 \text{ rad s}^{-1}$ ). The simulations are shown in Fig. 17 and confirm that the rigid wheel moves comparably to a rolling polygon and that hub movements are reduced for compliant spokes. Repeating the experiment at higher wheel velocities demonstrates another advantage of compliant spokes: Contact forces are applied gradually and shock loads are absorbed. This leads to further reduced hub movements at high speeds as the contacts occur fast enough for the wheel to stay practically at the same height between contacts due to inertia. The rigid wheel on the other hand starts to bounce around uncontrollably after reaching a certain velocity. This is due to sudden contact forces that are instantly applied to the wheel's centre of mass in the hub. A simulation for the compliant spoke at higher speeds is shown in Fig. 18. The Radial Spring Model was then simulated with a radial stiffness derived from an analogy to the harmonic oscillator [22]:

$$c_r = \frac{4}{3} m n^2 \omega_{ho}^2 \quad (19)$$

$$\omega_{wheel} = \omega_{ho} \sqrt{(1 - D^2)}, \quad (20)$$

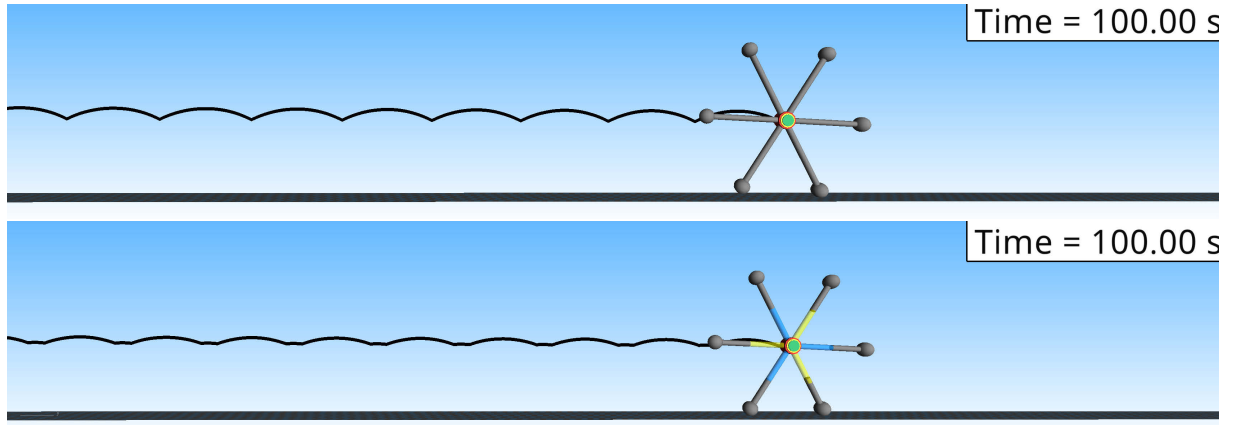


Figure 17: Quasi-static hub movements ( $\omega = 0.1 \text{ rad s}^{-1}$ )

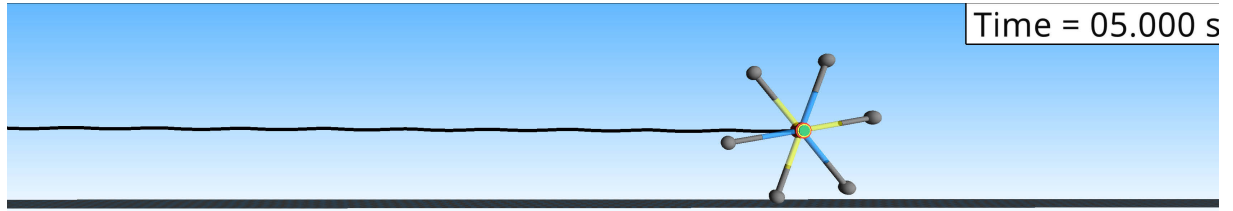


Figure 18: Hub movements at high angular wheel velocities ( $\omega = 14 \text{ rad s}^{-1}$ )

where  $m$  is mass,  $n$  is the number of spokes per wheel,  $\omega_{\text{ho}}$  is the harmonic oscillator's eigenfrequency,  $\omega_{\text{wheel}}$  is the wheel's resulting angular velocity and  $D$  is damping ratio. This relation indicates a value for the effective radial stiffness at different operating speeds.

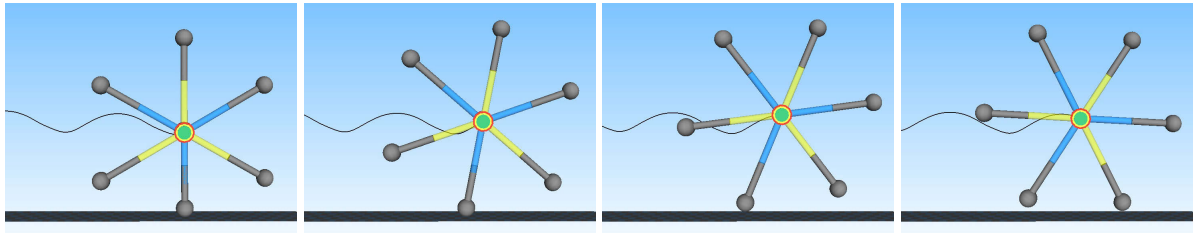


Figure 19: Radial Spring Model in resonance

The simulation shows that the analogy to a harmonic oscillator is valid but it was concluded that a purely radial spring is not the optimal approach to improve the efficiency of rimless wheel locomotion. The desired direction of movement is forward but storage of kinetic energy mostly occurs in the vertical direction, see Fig. 19. Here a segmented spoke design has a favourable morphology. The torsion spring adds a tangential stiffness to the wheel that allows the storage of mechanical energy in the direction of interest. This is the main reason that the Torsion Spring Model is favoured over the Radial Spring Model. Additional reasons include the increased energy storage in springs with a degressive stiffness characteristic and the simplified mechanical design through the similarity to the Continuous Beam Model.

## 5. PARAMETER VARIATION

The non-linear stiffness of the Torsion Spring Model prohibits analytical approaches to model its dynamics. Additionally, it is crucial to find a stiffness characteristic that works well for a range of angular wheel velocities. Thus, a parameter variation was set-up to simulate the rimless wheel based on segmented spokes at a number of angular velocities ( $\omega \in \{0.5 \text{ rad s}^{-1}, 3 \text{ rad s}^{-1}, 5 \text{ rad s}^{-1}, 8 \text{ rad s}^{-1}, 11 \text{ rad s}^{-1}, 14 \text{ rad s}^{-1}\}$ ), where the highest wheel velocity corresponds to an expected speed of the robot of  $2 \text{ m s}^{-1}$  (with  $15 \text{ cm}$  spokes). Spring stiffness and segment

angle ( $\beta_0 = 180^\circ - \varphi_{20}$ ) were varied in a wide range in steps of five ( $c_t \in [5 \text{ N m rad}^{-1}, 100 \text{ N m rad}^{-1}]$ ,  $\beta_0 \in [90^\circ, 175^\circ]$ ). A total of 2160 model variations were simulated which took a standard workstation computer approximately 2 days of wall clock time.

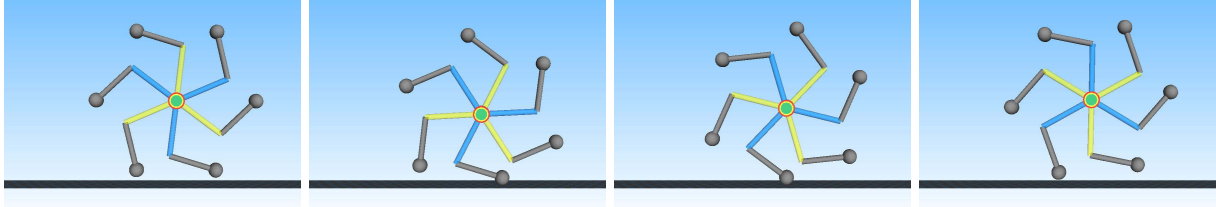


Figure 20: A simulation with an increased forward velocity due to dynamic movement ( $\omega = 5 \text{ rad s}^{-1}$ ,  $\beta_0 = 100^\circ$ ,  $c_t = 30 \text{ N m}^{-1}$ )

The simulation results were evaluated in terms of the average forward speed during the second half of the simulation ( $t = 10 - 20 \text{ s}$ ) when the wheel has settled into a periodic motion. The forward speed was normalised to facilitate a comparison between results at different wheel velocities. The normalisation was done with reference to the purely kinematic speed based on the evaluation of a rolling polygon, see Equation 1. Fig. 21 shows the simulation results for each simulated angular wheel velocity. The results can be grouped into slow, medium and fast simulations. For most of the slow simulations ( $\omega = 0.5 \text{ rad s}^{-1}$  and  $\omega = 3 \text{ rad s}^{-1}$ ) the forward speed is very close to the expected value of one. It is bigger than one for some spokes of small stiffness which is due to an “opening of the spoke” during the second half of every step. This increases the effective spoke length and therefore step length. There are regions of increased forward speed due to spoke dynamics for both simulations at medium velocities ( $\omega = 5 \text{ rad s}^{-1}$  and  $\omega = 8 \text{ rad s}^{-1}$ ). This can be attributed to the dynamic storage of mechanical energy described before. The spoke is loaded at impact and releases the stored energy during the second half of the step. Due to the wheel rotation and spoke kinematics, the direction of the force changes and is thus pushing the wheel forward. Frames from one simulation at  $\omega = 5 \text{ rad s}^{-1}$  are shown in Fig. 20. Normalised forward speed is below one for the whole parameter space in the fast simulations ( $\omega = 11 \text{ rad s}^{-1}$  and  $\omega = 14 \text{ rad s}^{-1}$ ). This is due to increased slippage and the more frequent occurrence of jumps due to the high amount of energy in the system.

The final set of parameters for the prototype is chosen based on the multiplied results of each

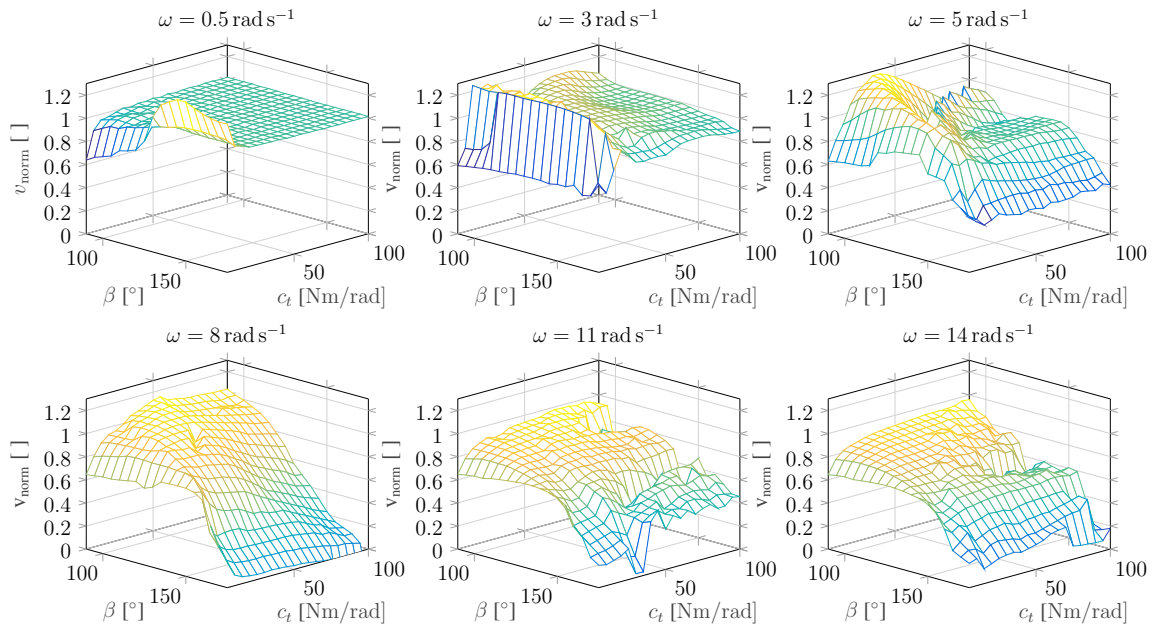


Figure 21: Detailed results of the parameter variation

wheel velocity. This approach ensures that the chosen design works well for a wide range of velocities. The final parameter set ( $c_t = 35 \text{ N m rad}^{-1}$  and  $\beta_0 = 100^\circ$ ) was chosen to be in the beneficial range in the left of Fig. 22. Here the wheel moves faster than kinematically expected at medium velocities and performs well at increased velocities, too. Thus the parameters were chosen to be a compromise between the behaviour at different speeds, rather than the total optimum. Furthermore, additional simulations have shown that the chosen parameters enable the system to be robust with respect to changes in system mass up to a factor of 2, still enabling dynamic storage of energy. This allows to reuse existing designs for higher payload demands or different gravitational environments.

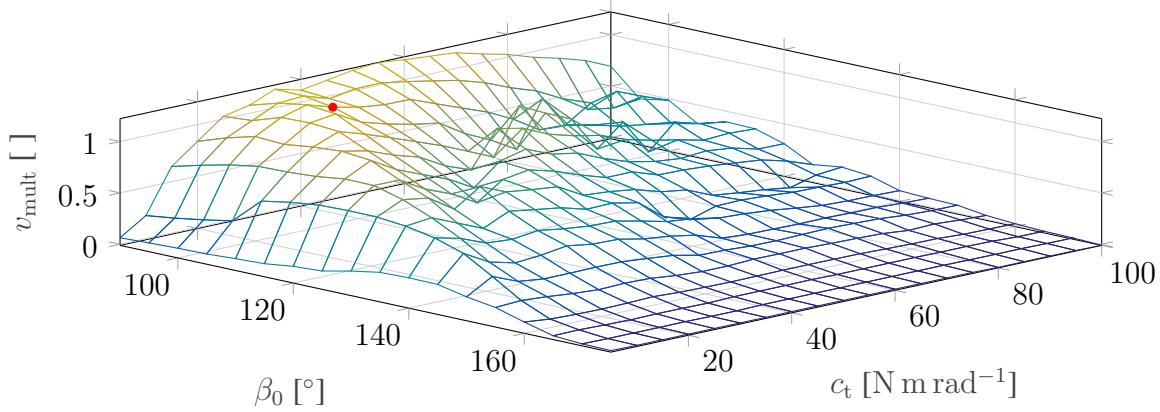


Figure 22: Parameter variation results

## 6. WHEEL DESIGN BENCHMARKS

A simulation of a full robot with six wheels was set-up to test the chosen parameter set in more realistic environments. For these simulations the robot was split into three segments that are connected by compliant elements in the roll and pitch directions. The bending between segments allows the robot to adapt its shape to rough terrain to increase traction and avoid beaching. The simulations are depicted in Fig. 23 and show that a robot equipped with rimless wheels is able to surmount a flight of stairs and climb inclined rough terrain. The flight of stairs has been successfully mastered in both, tripod and synchronous mode. Similar to the results for the single wheel, it was beneficial to run the rover in backwards direction to get better grip on the stairs. The rough terrain was created in such a way, that the size of bumps, dents and potholes is comparable to the terrain in both volcanic lava-fields and lava-tubes. Additionally the inclination is increasing with the driven distance up to a maximum inclination found to be the maximum in the eruptive fissure of Grotta dei Tre Livelli on Mt. Etna [26]. The created terrain was supposed to stop the rover at a certain point, giving the ability to rate the performance by the distance covered. However the rover was able to reach the top in most simulated speeds, resulting in the need to create even more extreme terrains for ongoing full system optimizations. The simulations therefore increase the confidence that the designed wheel is suitable for challenging terrain in real-world scenarios and might be suitable for even further complicated terrain than originally intended.



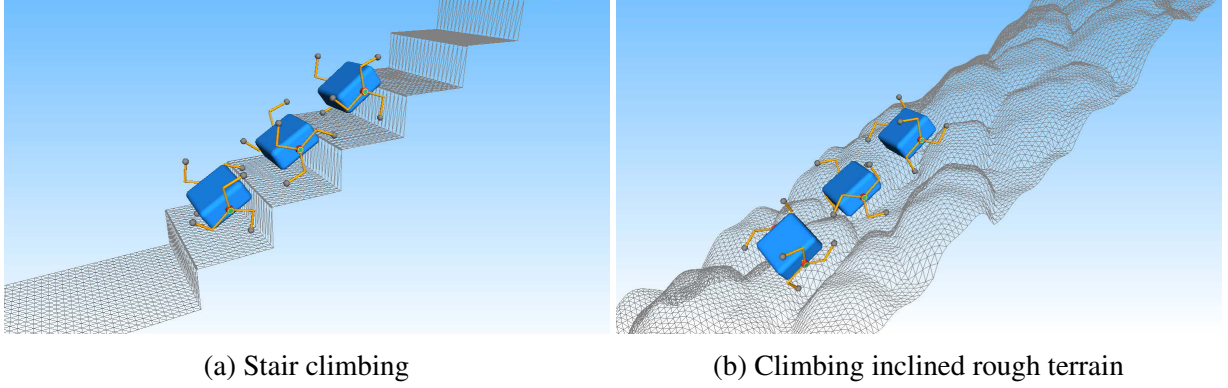


Figure 23: Benchmark obstacles

## 7. LOCOMOTION IN SOFT SOILS

In order to confirm the assumption of increased traction of the rimless wheel in soft soils and to properly size the wheel in terms of traction, both analytical and numerical soil modelling has been carried out. Thereby a simple model based on RANKINE's soil pressure [27] has been used to size the width of the spokes [22]. Given the soil forces on the spoke  $F_p$  and the frictional forces  $F_R$  on the body:

$$F_R = \mu_{\text{body}} m_{\text{body}} g \quad (21)$$

$$F_p = \frac{n_{\text{wheels}}}{2} \rho g K_{\text{ph}} b h^2, \quad (22)$$

spoke width  $b$  can directly be derived by:

$$F_R < F_p \quad (23)$$

$$b > \frac{2\mu_{\text{body}} m_{\text{body}}}{n_{\text{wheels}} \rho K_{\text{ph}} h^2}, \quad (24)$$

where  $\mu_{\text{body}}$  is the friction coefficient between soil and body,  $m_{\text{body}}$  is body mass,  $n_{\text{wheels}}$  is the number of wheels,  $K_{\text{ph}}$  is passive soil pressure coefficient,  $\rho$  is soil density and  $h$  is the height of the spoke's cross section. Inserting suitable estimations yielded a minimum spoke width of  $b = 44 \text{ mm}$ .

In order to verify that the width is suitable, the Discrete Element Method (DEM) is applied. The numerical simulations are based on the models shown in [28] and carried out in a DLR simulation tool (partsival) on the GPU. The model soil is a very soft soil impassable for wheels of similar size. Fig. 24 shows several states of the simulation with about 500000 particles after the wheel has reached steady state conditions. Due to massive parallelisation on the GPU the simulation of 1 m of travel at  $5 \text{ rad s}^{-1}$  took only several hours to complete. In frame 1 in Fig. 24 the front spoke just enters the soil and slows the wheel down, while in frame 2 the same spoke starts to create tractive forces, continuing during frame 3–7. Thereby the previous spoke outcrops some soil, which is dropped again in frames 7 and 8. In frame 7 the next spoke enters the soil restarting the cycle in frame 8. It is noticeable, that even though the wheel sinks about one times the radius, it is still able to move, see also Fig. 25. This is due to the lift forces that are exerted once a spoke enters the soil creating a swimming motion through the soil. Regarding slip no values higher than 60 % were observed during the simulations. Further simulations on common soils like the quartz simulant WF34 [29] showed only partial sinkage of the spokes and even lower slip values. The simulations have been based on validated models [29] and have additionally been compared to recent tests of the rimless wheel prototype with good correspondence of the observed effects.

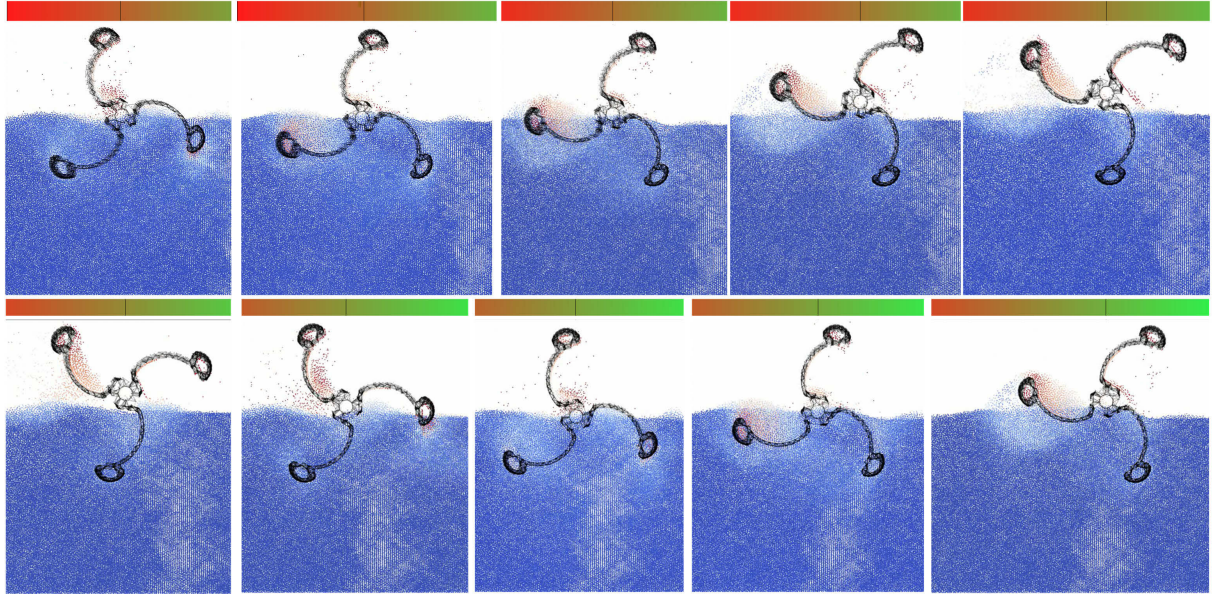


Figure 24: DEM simulation of the rimless wheel; The progress of the wheel position is indicated on the colorbar



Figure 25: DEM simulation of the rimless wheel; state after 6 m of driving

## 8. THE PROTOTYPE

A prototype is designed based on the Continuous Beam Model using the fitting process described earlier in section 3. The spoke's monolithic design distributes the bending stresses along the beam and poses fewer single points of failure than a design consisting of multiple elements. A monolithic spoke is therefore more robust, lighter and simpler to manufacture as it integrates functional and structural parts. The fitting of the stiffness characteristic is executed using a Matlab script that calculates both models simultaneously and changing the values of  $h$  and  $r$ , minimising the error. The resulting curve for a beam made from Polyoxymethylene (POM,  $E_{\text{POM}} = 2.6 \text{ GPa}$ ) is shown in Fig. 26. Its dimensions are  $b = 44 \text{ mm}$ ,  $h = 6 \text{ mm}$  and  $r = 82 \text{ mm}$ . In the area of expected loads (up to  $250 \text{ N}/40 \text{ mm}$ ) the fitting process yielded very good results.

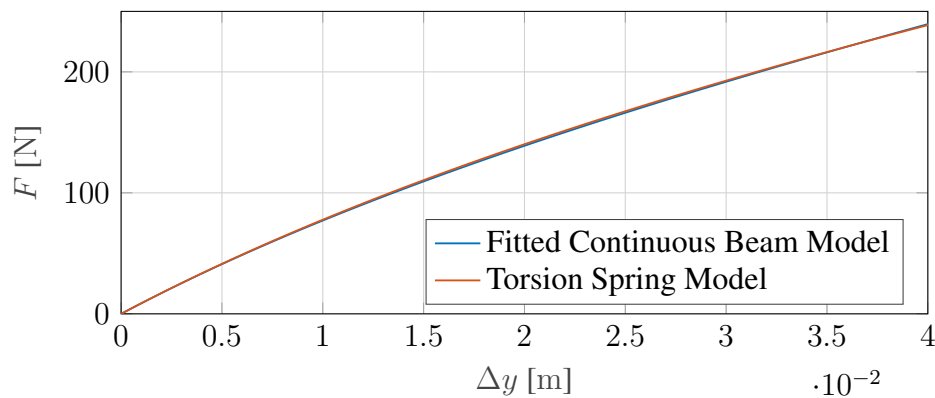


Figure 26: Matching the radial force characteristic of a curved beam made of POM to the resulting spoke from the parameter variation

The same procedure was conducted for a spoke made from spring steel (51CrV4), which is a material applicable in space. Due to the higher YOUNG's modulus the beam based on spring steel has a narrower cross section ( $E_{\text{steel}} = 206 \text{ GPa} \rightarrow h = 1.4 \text{ mm}$  and  $b = 44 \text{ mm}$ ). The material of choice for the prototype is POM as it is cheaper and easier to manufacture in small quantities. The maximum radial deflection of the chosen model during the parameter variation was 33 mm which corresponds to a radial force of 207 N. A stress analysis was conducted for this point to ensure the spoke's structural integrity during operation. In the case of the spoke made from POM these calculations yielded occurring stresses of  $49.8 \text{ N mm}^{-2}$  which are lower than the upper limit of acceptable stresses of  $62.5 \text{ N mm}^{-2}$ , calculated with a safety factor of  $S_F = 1.2$ . For the spoke made from spring steel these values are  $913.7 \text{ N mm}^{-2}$  and  $1200 \text{ N mm}^{-2}$ , respectively. Implementing this beam model into a physical spoke entails trade-offs. Due to the required hub diameter the spoke's elastic length had to be reduced, see Fig. 27. Every spoke is equipped with an elastic foot to soften contacts, provide better grip during climbs and increase traction on granular media. Additionally the soft rubber foot provides the needed contact damping, which was also included in the contact model. For POM and spring steel different material damping is to be expected, whereas the simulations had been carried out with the values for POM. Thus for usage of spring steel measures to increase damping shall be taken.

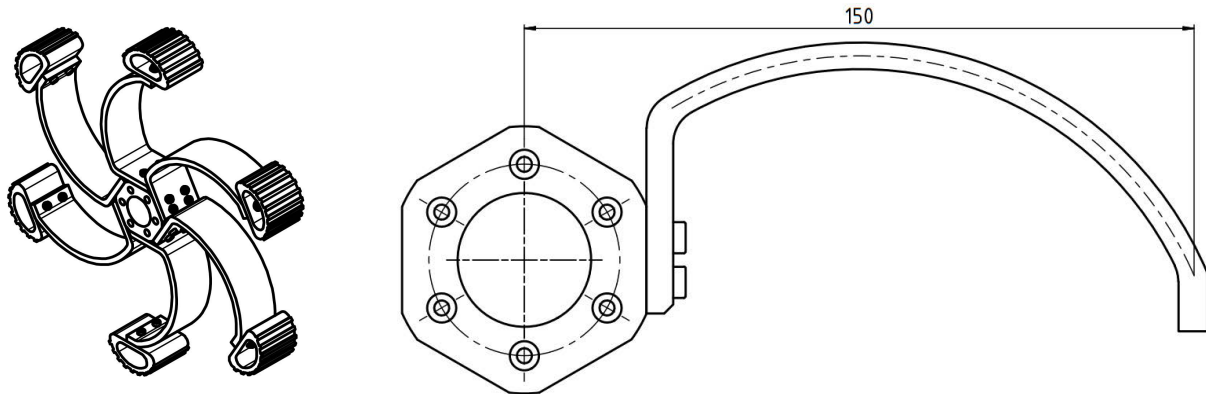


Figure 27: A sketch of the prototype of a six spoked wheel, modeling an axis of two three spoked wheels, and a side view of the hub and one spoke

## 9. EXPERIMENTS

The prototype is tested with respect to the occurring reaction forces to provide a first validation of the mechanical models. Tests are conducted on DLR-SR's novel robotic testbed, called the "Terramechanics Robotic Locomotion Laboratory" (TROLL). It is based on an industrial robot from KUKA that is equipped with a motor and a force-torque sensor. This allows for the wheel to be moved on free, force controlled trajectories while measuring forces and torques in addition to prescribed rheonomic motions. Due to the highly dynamic behaviour of the systems with alternating open and closed contacts, the force control could not be used. Thus fixed slip tests on a pre-defined hub height are carried out. It shall be noted, that due to this fact the tests do not directly give information on the locomotion capability and shall be used for validation of the models, only. The multi-body simulation was adapted to use pre-defined trajectories based on averages from the dynamic simulation to provide a valid comparison. Additionally, the motor torque from this adapted simulation is used as an input of the analytical mechanical model for the segmented spoke.

The height of the wheel above the test track, an aluminium profile, was determined in a preliminary experiment where the wheel was moved downward until the spoke's deformation matched



the maximum deformation during the adapted simulation. This approach in combination with the low stiffness of the elastic feet limits their influence on the reaction forces. Experiments were conducted for the three slower angular wheel velocities ( $\omega = \{0.5 \text{ rad s}^{-1}, 3 \text{ rad s}^{-1}, 5 \text{ rad s}^{-1}\}$ ). A frame sequence from one of the experiments at  $\omega = 0.5 \text{ rad s}^{-1}$  is shown in Fig. 28. The ground contacts overlap due to the size of the feet.

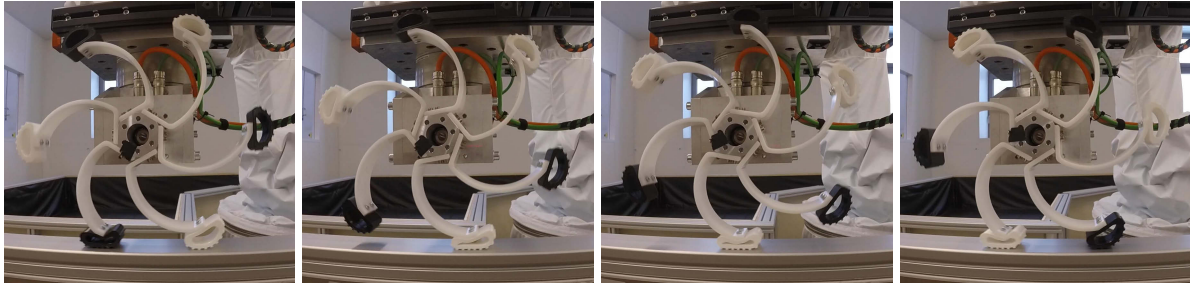


Figure 28: Frames showing one step of the prototype ( $\omega = 0.5 \text{ rad s}^{-1}$ )

Fig. 29 shows the reaction forces of mechanical model, multi-body simulation and experiment for one step of the rimless wheel at  $\omega = 3 \text{ rad s}^{-1}$ . The plots for the mechanical model and the measurement have been scaled in  $y$  to show one zero-crossing of the forward force  $F_y$ . The shown measurement plot is the average of four experiments.

Comparing the forces many similarities but also a number of differences can be found. The vertical force  $F_z$  increases as soon as a contact is found and the spoke is loaded. Vertical force peaks roughly at the middle of the step and then decreases during the step's second half. The peak force during the experiment is 16 % lower than the vertical force at that point of the analytical model and the simulation. This is due to the spoke being less stiff than the model ( $\approx 8 \%$ ), which was measured in a separate experiment. In addition, the height of the wheel above the test track may have been set inaccurately and is suspected to having introduced an error. For the mechanical model and the MBS the vertical force falls to zero in between steps. For the prototype this is not the case because contacts overlap. This also causes the forward force in the experiment to be considerably lower ( $\approx 50 \%$ ) than for the two models because the reaction forces of the two feet in contact superpose. All three plots exhibit the same trend and timing. Forward force is positive during the first part of the step, when the spoke is loaded. During the second part the spoke decompresses and gives the wheel a push forward ( $F_y < 0$ ). The regular ripples in the measurement can be related to the elastic feet which have a corresponding number of treads. Other differences between mechanical model, multi-body simulation and experiment can be explained by dynamic effects, such as damping, contacts and inertia.

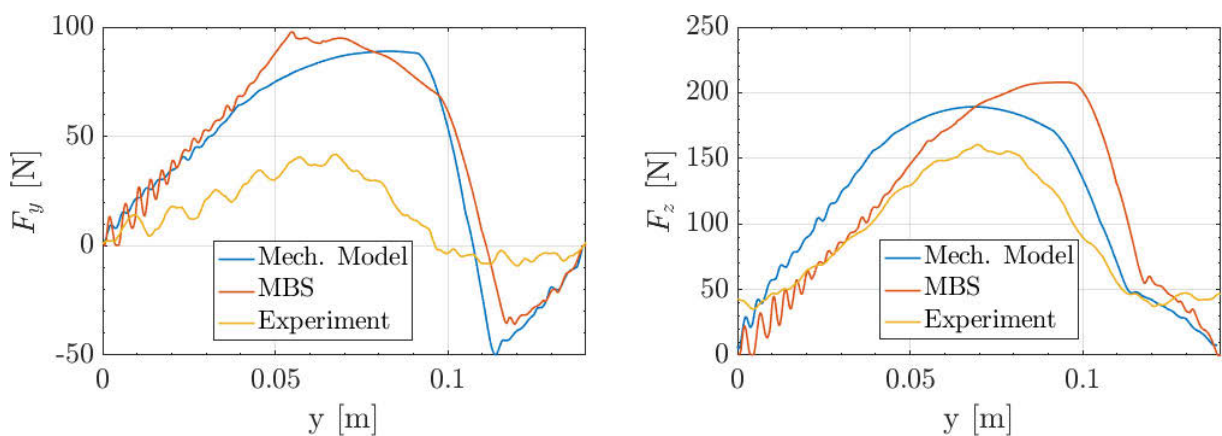


Figure 29: Comparison of models and measurement

## 10. CONCLUSION

In this work a locomotion system for a future scout rover based on compliant rimless wheels was developed, modelled and designed. For this purpose analytical models of the rimless wheel's kinematics were set-up and examined. The use of compliant spokes was found to be beneficial and lead to three models of compliant spokes. The dynamic behaviour of rigid and compliant rimless wheels was investigated using computational multi-body simulations. A suitable set of parameters for the future scout rover was found by means of a parameter variation and implemented in a wheel prototype. Testing the prototype provided a first validation of both the analytical model and the multi-body model as the observed reaction forces agree with minor qualitative differences due to design specifics of the prototype. Using simple and complex models for the interaction with soft soils proved the ability to overcome patches of extremely soft soil. In conclusion, the results provide strong support that the two-sided goal of efficient movement on hard and flat surfaces as well as reliable negotiation of rough terrain can be achieved with the developed locomotion system.

A range of future work around the topic of compliant spokes can be derived from this project. More detailed models including for example the foot's two-dimensional stiffness will further improve the agreement between simulation and experiment. Furthermore the beam model will be used directly inside the MBS and dynamic effects of the deformation shall be covered. The beam model's radial stiffness is dependent on the spoke's actuation. Depending on the spoke's orientation, it is bent up or down by a motor torque. Using this effect it is possible to tune the wheel dynamics under load to maximise energy storage and increase the system's efficiency. An adapted motor controller can be employed to increase efficiency in another way. The position control used during simulation and testing makes the motor act against the direction of movement for a fraction of every step. Electrical energy can be saved by letting the decompressing spoke push the robot freely. A quantitative energy analysis of the full robot will assist the research of these opportunities for efficiency improvements. For future experiments the force control algorithm of the TROLL facility should be adapted to allow for free slip tests with opening and closing contacts. Using these free slip tests further validation on hard as well as soft ground (sand) shall be performed. As a last point full system optimization is needed to properly choose the parameters of spine stiffness and to determine the sizes of the full system.

## REFERENCES

- [1] NASA/JPL, "Super Resolution Stereo Pairs of "Twin Peaks" by Dr. Timothy Parker, JPL." <http://mars.nasa.gov/MPF/parker/highres-stereo.html>, 1998. Accessed: 2017-02-17.
- [2] A. Seeni, B. Schäfer, and G. Hirzinger, "Robot Mobility Systems for Planetary Surface Exploration – State-of-the-Art and Future Outlook: A Literature Survey," *Aerospace Technologies Advancements*, pp. 978–953, 2010.
- [3] R. R. Vondrak and D. H. Crider, "Ice at the Lunar Poles: That the Moon harbors ice at high latitudes is well known. The source of that water, however, may come as something of a surprise," *American Scientist*, vol. 91, no. 4, pp. 322–329, 2003.
- [4] G. E. Cushing and T. N. Titus, "Caves on mars: Candidate sites for astrobiological exploration," *LPI Contributions*, vol. 1538, p. 5414, 2010.
- [5] C. M. Angle and R. A. Brooks, "Small planetary rovers," in *IROS'90. IEEE International Workshop on Intelligent Robots and Systems*, pp. 383–388, IEEE, 1990.

- [6] E. Allouis, R. Marc, G. J., *et al.*, “Faster project-demonstration of multi-platform operation for safer planetary traverses,” 2015.
- [7] P. A. Dunker, W. A. Lewinger, A. J. Hunt, and R. D. Quinn, “A biologically inspired robot for lunar in-situ resource utilization,” in *2009 IEEE/RSJ International Conference on Intelligent Robots and Systems*, pp. 5039–5044, IEEE, 2009.
- [8] J. Schwendner, F. Grimminger, S. Bartsch, T. Kaupisch, M. Yüksel, A. Bresser, J. B. Akpo, M. K.-G. Seydel, A. Dieterle, S. Schmidt, *et al.*, “Cesar: A lunar crater exploration and sample return robot,” in *2009 IEEE/RSJ International Conference on Intelligent Robots and Systems*, pp. 3355–3360, IEEE, 2009.
- [9] R. U. Sonsalla, J. B. Akpo, and F. Kirchner, “Coyote III: Development of a modular and highly mobile micro rover,” in *Proc. of the 13th Symp. on Advanced Space Technologies in Robotics and Automation (ASTRA)*, 2015.
- [10] S. Sand, S. Zhang, M. Mühlegg, G. Falconi, C. Zhu, T. Krüger, and S. Nowak, “Swarm exploration and navigation on mars,” in *International Conference on Localization and GNSS (ICL-GNSS), 2013*, pp. 1–6, IEEE, 2013.
- [11] M. Gerner, T. Wimbock, A. Baumann, M. Fuchs, T. Bahls, M. Grebenstein, C. Borst, J. Butterfass, and G. Hirzinger, “The DLR-Crawler: A testbed for actively compliant hexapod walking based on the fingers of DLR-Hand II,” in *IEEE/RSJ International Conference on Intelligent Robots and Systems, 2008. IROS 2008.*, pp. 1525–1531, IEEE, 2008.
- [12] B. Yeomans and C. M. Saaj, “Progress towards robust mobility analysis for a legged planetary fetch rover,” in *Proceedings of 11th Symposium on Advanced Space Technologies in Robotics and Automation (ASTRA)*, 2011.
- [13] S. Köhring and F. Becker, “Das rollende Bein – eine Kombination aus Rollen und Schreiten für die Nahfeldmobilität,” *Konstruktion*, 2013.
- [14] R. D. Quinn, J. T. Offi, D. A. Kingsley, and R. E. Ritzmann, “Improved mobility through abstracted biological principles,” in *IEEE/RSJ International Conference on Intelligent Robots and Systems*, vol. 3, pp. 2652–2657, IEEE, 2002.
- [15] R. Altendorfer, N. Moore, H. Komsuoglu, M. Buehler, H. Brown, D. McMordie, U. Saranli, R. Full, and D. E. Koditschek, “RHex: A biologically inspired hexapod runner,” *Autonomous Robots*, vol. 11, no. 3, pp. 207–213, 2001.
- [16] J. Mämpel, S. Köhring, R. Koopmann, K. Langguth, R. Lichtenheldt, and H. Witte, “ROLV – A Hybrid Wheel Robot Using Compliant Mechanisms for Locomotion,” *The 5th International Symposium on Adaptive Motion of Animals and Machines*, pp. 23–24, 2011.
- [17] T. McGeer, “Passive dynamic walking,” *The International Journal of Robotics Research*, vol. 9, no. 2, pp. 62–82, 1990.
- [18] J. E. Pratt and G. A. Pratt, “Exploiting natural dynamics in the control of a planar bipedal walking robot,” in *Proceedings of the Annual Allerton Conference on Communication Control and Computing*, vol. 36, pp. 739–748, 1998.
- [19] J. Rummel and A. Seyfarth, “Stable running with segmented legs,” *The International Journal of Robotics Research*, vol. 27, no. 8, pp. 919–934, 2008.
- [20] D. E. Koditschek, R. J. Full, and M. Buehler, “Mechanical aspects of legged locomotion control,” *Arthropod structure & development*, vol. 33, no. 3, pp. 251–272, 2004.
- [21] L. Zentner, *Nachgiebige Mechanismen*. Walter de Gruyter GmbH & Co. KG, 2014.

- [22] L. Stubbig, “Modellbasierte Entwicklung eines mobilen Scouts für extreme Gelände in der planetaren Exploration (Model-based development of a mobile scout for extreme terrain in planetary exploration) [in English],” Bachelor’s Thesis, TU Ilmenau, 2017.
- [23] R. Blickhan, “The spring-mass model for running and hopping,” *Journal of biomechanics*, vol. 22, no. 11-12, pp. 1217–1227, 1989.
- [24] M. J. Coleman, A. Chatterjee, and A. Ruina, “Motions of a rimless spoked wheel: a simple three-dimensional system with impacts,” *Dynamics and stability of systems*, vol. 12, no. 3, pp. 139–159, 1997.
- [25] Simpack Release 9.9, Simpack GmbH, Weßling, Germany, “Documentation,” 2015.
- [26] R. Bonaccorso and R. Maugeri, “Ten of the most interesting caves on mount etna. cadastral files,” in *IXth International Symposium on Vulcanospeleology*, 1999.
- [27] H. Türke, *Statik im Erdbau*. Ernst & Sohn, 2nd ed., 1990.
- [28] R. Lichtenheldt, *Lokomotorische Interaktion Planetarer Explorationssysteme mit weichen Sandböden – Modellbildung und Simulation*. PhD thesis, TU Ilmenau, 2016.
- [29] R. Lichtenheldt, B. Schäfer, and O. Krömer, “Hammering beneath the surface of Mars – Modeling and simulation of the impact-driven locomotion of the HP3-Mole by coupling enhanced multi-body dynamics and discrete element method,” in *58th Ilmenau Scientific Colloquium (ISC)*, 2014.

## CONTACTS

Leon Stubbig, B.Sc.

Dr.-Ing. Roy Lichtenheldt

Dr.-Ing. Felix Becker

Univ.-Prof. Dr.-Ing. habil. Klaus Zimmermann

[leon.stubbig@tu-ilmenau.de](mailto:leon.stubbig@tu-ilmenau.de)

[roy.lichtenheldt@dlr.de](mailto:roy.lichtenheldt@dlr.de)

[felix.becker@tu-ilmenau.de](mailto:felix.becker@tu-ilmenau.de)

[klaus.zimmermann@tu-ilmenau.de](mailto:klaus.zimmermann@tu-ilmenau.de)